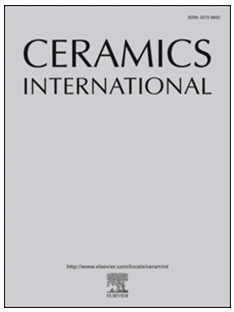

Assessment of mechanical properties at microstructural length scale of Ti(C,N)–FeNi ceramic-metal composites by means of massive nanoindentation and statistical analysis

H. Besharatloo, M. de Nicolás, J.J. Roa, M. Dios, A. Mateo, B. Ferrari, E. Gordo, L. Llanes

PII: S0272-8842(19)31805-X

DOI: https://doi.org/10.1016/j.ceramint.2019.06.292

Reference: CERI 22101

To appear in: *Ceramics International*

Received Date: 17 May 2019

Revised Date: 24 June 2019

Accepted Date: 27 June 2019

Please cite this article as: H. Besharatloo, M. de Nicolás, J.J. Roa, M. Dios, A. Mateo, B. Ferrari, E. Gordo, L. Llanes, Assessment of mechanical properties at microstructural length scale of Ti(C,N)–FeNi ceramic-metal composites by means of massive nanoindentation and statistical analysis, *Ceramics International* (2019), doi: https://doi.org/10.1016/j.ceramint.2019.06.292.

Assessment of mechanical properties at microstructural length scale of Ti(C,N)-FeNi ceramic-metal composites by means of massive nanoindentation and statistical analysis

H. Besharatloo[1,2,*], M. de Nicolás[3], J.J. Roa[1,2], M. Dios[3], A. Mateo[1,2], B. Ferrari[4], E. Gordo[3] and L. Llanes[1,3]

[1] CIEFMA - Department of Materials Science and Metallurgical Engineering, EEBE, Universitat Politècnica de Catalunya-BarcelonaTech, 08019 Barcelona, Spain

[2] Barcelona Research Centre in Multiscale Science and Engineering, Universitat Politècnica de Catalunya-BarcelonaTech, 08019 Barcelona, Spain

[3] GTP - Department of Materials Science and Engineering, Universidad Carlos III Madrid, Avda. De la Universidad, 30, 28911 Leganés, Spain.

[4] Institute of Ceramic and Glass, CSIC, 28049 Madrid, Spain

*Corresponding author, email: luis.miguel.llanes@upc.edu

Abstract

It is well known the interest of the scientific community in substituting the traditional cemented carbides (WC-Co) by alternative ceramic-metal systems. In this regard, Ti(C,N)-based cermets arise as excellent candidates due to their exceptional mechanical, tribological and thermal properties. In this work, microstructurally different Ti(C,N)-FeNi cermets were processed using a combination of colloidal and powder metallurgy techniques. Three distinct ceramic/metal phase ratios were used: 85/15, 80/20 and 70/30 (volume fraction) of Ti(C,N) and FeNi respectively. Microstructural parameters and micromechanical properties (hardness and stiffness) of the three composite systems and their constitutive phases were assessed. Small-scale hardness was evaluated by means of massive nanoindentation testing and statistical analysis of the gathered data, under the consideration of three mechanically different phases: Ti(C,N) particles, metallic binder and a composite-like one, corresponding to probing regions containing both constitutive phases. It is found that values of local hardness for both composite-like and metallic phases increase as the ceramic/metal phase ratio rises. In particular, local hardness values are determined to be significantly distinct for the metallic binder in the three cermets investigated. Results are discussed and rationalized on the basis of the constrained deformation imposed for the harder phase to the softer and more ductile one. Estimated effective flow stress values for the metallic binder as well as detailed inspection of crack-microstructure interaction and fractographic features point out the effectiveness of FeNi as reinforcement phase and toughening agent for Ti(C,N)-base cermets.

Keywords: Cermet, Nanoindentation, Massive indentation, Statistical analysis.

1. Introduction

Cemented carbides are a group of ceramic-metal composite materials with exceptional combinations of hardness, strength and toughness together with unique wear and abrasion resistance [1,2]. Main reasons behind it are the wide range of microstructural assemblages available for these composites, all of them consisting of interpenetrating networks of two phases with completely different properties: hard/brittle ceramic particles and soft/ductile metallic binder [3–5]. Among these materials, WC-Co alloys, also referred to as hardmetals, are one of the most successful "tailor-made" composites. As a result, they are nowadays preeminent material choices for extremely demanding applications, such as metal cutting/forming or mining tools, where high performance and reliability levels are required [6]. However, in recent years both scientific and industrial sectors have been struggling to find substitution materials for these reference WC-Co cemented carbides. This is mainly because the classification of cobalt and tungsten as critical raw materials by the European Union (i.e. besides being considered as raw materials of a high importance to the economy of the EU, there exists a high risk of a disruption in their supply), as well as their consideration as hazardous substances for human health [7–9].

Following above ideas, Ti(C,N)-based ceramic-metal systems (cermets) have been proposed as competitive alternative systems to plain WC-Co alloys, owing to their outstanding hardness, oxidation and wear resistance, as well as thermal and chemical stability [10–13]. With respect to the metallic constituent, Fe and Ni alloys are both considered to substitute Co. The lower price and non-toxicity state of Fe compared to Co, make it a proper option as a metallic binder. Furthermore, Fe is an abundant raw material

and has the ability to be hardened by thermal treatments [14–16]. Meanwhile, Ni becomes an optimal alloying element, as previous studies have demonstrated that it improves the wettability between Fe and Ti(C,N), a behaviour directly related to the densification of the samples during the sintering stage [17]. Nevertheless, high functional performance levels exhibited by hardmetal tools and components require, besides achievable processing, similar exceptional hardness-toughness correlations. Thus, both intrinsic hardness of ceramic particles and effective toughening by the metallic binder become key microstructural design parameters for designing and developing new ceramic-metal systems.

Although there exist a large amount of studies on mechanical properties of ceramic-metal systems (either WC- or Ti(C,N)-based), they have been mainly addressed to evaluate basic and macroscopic parameters, i.e. Vickers hardness and/or Palmqvist indentation fracture toughness [18–22]. On the other hand, research focused on small-scale hardness/toughness, i.e. at the level of microstructural dimensions, has been rather limited and mainly focused on WC-based systems [23–32]. In this regard, as it has been recently validated by the authors, massive nanoindentation together with statistical analysis of the gathered data have shown to be a quite effective micromechanical testing protocol for experimental assessment and understanding intrinsic mechanical properties of main constitutive phases, especially those of the constrained binder [25,27,32]. Within this framework, it is the objective of the present study to evaluate the small-scale mechanical properties for the main constitutive phases present on Ti(C,N)-FeNi composites exhibiting different ceramic/metal phase ratio. Results are expected to provide microstructural design guidelines for novel cemented

carbides aiming to satisfy mechanical and tribological requirements associated with increasingly demanding applications.

2. Experimental procedure

2.1. Sample preparation

Titanium carbonitride (Ti(C,N), Ti($C_{0.5}$,$N_{0.5}$)) and iron (Fe, Fe SM) submicron powders were supplied by H.C Starck (Germany). On the other hand, submicron powder of nickel (Ni, Ni 210H) was provided by INCO (Canada). Particle size and specific surface area were characterized by means of laser analyser (Mastersizer S, Malvern instruments Ltd., UK) and one-point N_2 absorption (Monosorb Surface Area, Quantachrome Corporation, USA), respectively. Moreover, Monosrb Multipycnometer (Quantachrome Corporation, USA) set was used to measure the density of the as-received powders. All the mentioned parameters are summarized in **Table1**.

Powders were processed using a combination of colloidal and powder metallurgy techniques. High solid content suspensions were formulated for submicron powders of Ti(C,N), Fe and the mixture of Fe and Ni, using deionized water as dispersion medium [33,34]. In all cases, the slurries were prepared in deionized water and pH was adjusted up to 10-11 adding Tetra methyl ammonium hydroxide (TMAH), where surfaces of the powder particles are chemically stable. Then the necessary amount of Polyethylenimine (PEI) to completely cover the particle surface in each case, was added as dispersant. Slurries of Ti(C,N) and the mixture of Fe and Ni powders were prepared and milled separately in a ball mill for 1 h, using Si_3N_4 and nylon balls, respectively.

Milling process was followed by the mixture of the Ti(C,N) and Fe/Ni slurries in order to get the desired powder compositions. The volume ratio of Ti(CN)/FeNi were 85/15, 80/20 and 70/30 vol/vol for each mixture. **Table 2** summarizes the volume and weight ratio of considered powder composition as well as the composition of the formulated metallic binder (85/15 wt/wt Fe/Ni) which was maintained constant in all cases. Then, 2 wt.% of Polyvinyl alcohol (PVA) was added as the processing polymer binder, and afterwards the slurry was kept for 20 min under mechanical stirring, before the spray-drying step.

Spray-dry method was implemented using stable aqueous suspensions of the mixture of powders to provide granules able to be pressed. This processing step allows the fabrication of a feedstock for pressing where ceramic and metal powders are homogeneously dispersed and mixed. In doing so, LabPlant SD-05 atomizer (North Yorkshire, UK) was used with the main controlled operating parameters being inlet and exhaust temperatures: 190ºC and 100ºC respectively. The slurry pump rate (2 L/h) and the atomizing nozzle design were set to attain spherical agglomerates with high compressibility, capable to be formed by uniaxial pressing [34]. Finally, a uniaxial die was used to press the granules into disks (16 mm in diameter) at 600 MPa. Compressed samples were sintered in a high-vacuum furnace (10^{-5} bar) for 2 hours at 1450ºC, with a dwell time of 30 min at 800ºC.

In order to correctly prepare sample surfaces for microstructural and micromechanical characterization, cross sections of the sintered materials were polished precisely with

diamond paste down to 3 µm. Polishing by colloidal alumina was conducted as final step, in order to release any work-hardening effect induced in the metallic binder during previous sample preparation stages.

2.2. Microstructural characterization

Microstructural characterization included the evaluation of grain size of the carbonitride phase ($d_{Ti(C,N)}$), mean free path (λ) of the metallic binder and porosity. The former two parameters were assessed on images obtained in a field emission scanning electron microscopy (FESEM) unit (JSM-7100F, JEOL Ltd., Japan) at the acceleration voltage of 20 kV. Five micrographs per specimen were used and values were determined by means of the linear interception method (LIM) [35]. On the other hand, amount of porosity was determined, as a function of volume fraction of the metallic binder, by means of ImageJ software.

2.3. Small-scale mechanical characterization

Nanoindentation technique was implemented to evaluate the composite hardness *(H)* and elastic modulus *(E)* of Ti(C,N)-FeNi systems as well as the intrinsic hardness for each constitutive phase at both micro- and nanometric length scales, respectively. Nanoindentation tests were performed using a testing unit (Nanoindenter XP, MTS Systems Corporation, USA) coupled with a continuous stiffness measurement (CSM)

modulus. The set was equipped with a diamond Berkovich indenter, which was precisely calibrated by using a fused silica standard sample with a known Young's modulus, 72 GPa [36]. The micromechanical properties were extracted directly by using the Oliver and Pharr method [36,37].

In order to determine *H* and *E* of the composite system (Ti(C,N)-FeNi), an homogeneous array of 16 indentations (4 by 4) was performed at 2 µm of maximum penetration depth or until reaching the maximum applied load of the loading cell, 650 mN. On the other hand, aiming to evaluate the intrinsic hardness of each constitutive phase, 2000 indentations per sample (five matrices of 20 by 20) were done at a maximum displacement into surface of 200 nm. In this testing protocol, residual imprints and plastic flow need to be confined inside each phase, in order to guarantee that each single indentation could be considered as an individual statistical outcome. Furthermore, the distance between imprints was required to be set adequately to avoid any overlapping effect of neighbouring imprints. Taking these testing requirements into consideration, distances between applied imprints at 2000 and 200 nm penetration depths were kept constant at 50 and 5 µm, respectively [25].

2.4. Statistical analysis

Intrinsic hardness of each constitutive phase was evaluated by using the statistical analysis of the gathered *H* data, as proposed by Ulm and co-workers [25,38–41]. In doing so, investigated specimens were considered to contain several *(i)* mechanically distinct phases.

In this regard, three main phases were contemplated for the studied system: Ti(C,N) particles, metallic binder and a third one representative of the case where plastic flows of ceramic and metal phases are interacting, i.e. composite-like response. This statistical analysis assumes that distribution (p_i) of interested mechanical properties (in this case hardness) of each constitutive phase follows a Gaussian distribution:

$$p_i = \frac{1}{\sqrt{2\pi\sigma_i^2}} \exp\left[-\frac{(H - H_i)^2}{2\sigma_i^2}\right] \quad \textbf{(1)}$$

where H_i is the arithmetic mean of all individual indentations (N_i) performed on each phase (i) and σ_i is the standard deviation. Then, the cumulative distribution function (CDF) using sigmoid shape error function, may be fit by the following expression:

$$CDF = \sum_{i}^{n} \frac{1}{2} f_i \operatorname{erf}\left[\frac{H - H_i}{\sqrt{2}\sigma_i}\right] \quad \textbf{(2)}$$

where f_i is defined as the relative fraction occupied by each constitutive phase. In order to acquire reliable values, several restrictions were programmed during the deconvolution process. In this regard, the total volume fraction of constitutive phase was fixed at 1, while the fitting process was set to finalize when the chi-square (χ^2) tolerance was less than 10^{-15}, with an ultimate coefficient of determination (R^2) of 0.9998. Additional and detailed information about the statistical method followed can be found in references [25,38–41].

In order to implement this protocol, three main critical parameters must be taken into account: *(I)* indentation size, *(II)* relative difference in hardness values between the constitutive phase, and *(III)* grid size. These three main parameters will be recalled as results are presented and discussed in the following sections.

2.5. Damage and fracture micromechanisms

Deformation, subsurface damage and fracture-related (crack-microstructure interaction) scenario induced by residual imprints were evaluated by scrutinizing contact surfaces through a dual beam FESEM/Focused Ion Beam (FIB) unit (Neon40 Crossbeam, Carl Zeiss MicroImaging GmbH, Germany). Regarding cross-section examination, prior to milling, a thin protective layer of platinum was deposited on the region of interest to circumvent any waterfall effect, which could affect the quality of the images. Current and acceleration voltage of Ga^{+} source were subsequently reduced down to a final polishing stage at 500 pA and 30 kV respectively. Finally, special attention was paid to discern fractographic features of the metallic binder on intentionally (and abruptly) broken sections of previously indented samples.

3. Results and discussions

3.1. Microstructural parameters

FESEM micrographs of studied samples are shown in **Figure 1**. The corresponding microstructural parameters are summarized in **Table 3**. Grain size for the ceramic phase followed bimodal distributions, although mean value was quite similar for all the samples. **Figure 2** shows a typical grain size histogram for the Ti(C,N) particles with a constant bin size of 100 nm. It was plotted from data measured for 675 different grains in the sample 85Ti(C,N)-15FeNi. Qualitative similar histograms were attained for the rest of the specimens studied. Two distributions are overlapped to the experimental values, corresponding to coarse and fine Ti(C,N) particles, in agreement with microstructural scenarios discerned in images shown in **Figure 1**.

As it can be appreciated in **Figure 1** and **Table 3**, porosity was between 1 and 3% for all the specimens. It was reduced and density reached values close to 99% for specimens with the highest volume fraction of metallic phase studied. Considering that all the specimens were sintered using same temperature and time conditions, lack of binder for embedding all the ceramic particles when the liquid phase is formed seems to be a plausible reason for the higher porosity levels attained for 85/15 and 80/20 ceramic/metal phase ratios [17,34]. Nevertheless, it should be highlighted that, besides sintering temperature and time, there are additional processing variables that could affect final density of specimens. Achievement of

full density for every composition studied was out of the scope of this investigation, although it is a topic being addressed in ongoing research carried out by the authors.

3.2. Small-scale mechanical properties

3.2.1. Mechanical properties of the composite: Hardness and elastic modulus

Representative curves of measured hardness (*H*) and elastic modulus (*E*) values as a function of the displacement into the surface for the different Ti(C,N)-FeNi systems are shown in **Figure 3a** and **Figure 3b**, respectively. Possible indentation size effect (ISE) or tip defect interactions were evaluated by plotting the ratio between applied load and stiffness squared (P/S^2) as a function of the displacement into surface (e.g. **Figure 4** for cermet 80Ti(C,N)-20FeNi). As it may be seen, P/S^2 becomes independent of indenter penetration after 200 nm of displacement into surface. Therefore, values for *H* and *E* assessed for $h \geq 200$ nm may be considered as intrinsic ones for the three cermets studied (see Refs. [23,42]). Small-scale mechanical properties evolution shown in **Figure 3** and data for *H* and *E* summarized in **Table 4** highlights an expected inverse correlation between mean free path of the metallic binder (directly related to ceramic/metal phase ratio) and both parameters. This is in accordance with trends observed for microstructural effects on macro hardness (i.e. evaluated at much higher applied load levels, i.e. 10 and 30 Kgf) for the cermets here studied (**Table 4,** which are in agreement with the Vickers hardness values reported in Ref [34]). Relative differences in hardness values listed in **Table 4** may be

accounted recalling the mechanistic models proposed by Nix & Gao [43], on the basis of geometrically necessary dislocation concepts, for rationalizing hardness-penetration depth correlation according to:

$$\frac{H}{H_0} = \sqrt{1 + \frac{h^*}{h}} \quad \textbf{(3)}$$

where H is the hardness for a given depth of indentation (h), H_0 is the hardness in the limit of the infinite depth and h^* is a characteristic length that depends on the shear modulus, H_0 and the shape of the indenter [43]. In this regard, implementation of Nix & Gao model was found to fit satisfactorily the experimental data for hardness values of studied system, measured under different levels of applied load.

3.2.2. Intrinsic hardness

Prior to perform massive indentation testing, it is necessary to do a discrete evaluation of the intrinsic H for each phase In this regard; typical curves of hardness evolution as a function of maximum displacement into the surface are presented in **Figure 5** for the 80Ti(C,N)-20FeNi composite system. They correspond to indentations whose residual imprints were either completely confined in a constitutive phase or probing both phases (including interfaces) simultaneously. There, H values for both individual phases and the composite itself are not only distinguishable, but also discerned to follow trends towards

plateau levels as penetration depth gets deeper than 100 nm. This supports above finding that mechanical response is not affected by any ISE for h ≥ 200 nm (see **Figure 4** [25,27]). Furthermore, additional inspection was done to assess imprint scenario at the subsurface level. **Figure 6a** and **Figure 6b** shows surface and FIB-milled cross-section views of a residual imprint in a Ti(C,N) particle respectively. It is evidenced that it is absolutely embedded within the ceramic phase. This will also apply for plastic field dimensions, estimated to range between 1.4 and 2.0 μm (i.e. between 7 and 10 times maximum displacement into the surface); thus, slightly smaller than the mean grain size determined experimentally by using the LIM (see **Table 3**) for the Ti(C,N) particles. These facts then point out the data gathered from 200 nm in-depth indentations as valid for implementing the statistical method to be used for extracting intrinsic hardness values of individual phases for cermets here investigated.

3.2.3. Massive nanoindentation testing and statistical analysis

Figure 7 shows a small-cropped region of the indentation arrays of 2000 imprints performed at 200 nm of maximum penetration depth, as observed by FESEM. The related hardness histogram, with a constant bin size of 1 GPa, for sample 85Ti(C,N)-15FeNi is presented in **Figure 8.** Three discrete peaks with mean values of 19, 27 and 34 were determined. The highest and lowest peaks are attributed to the intrinsic hardness of ceramic and metallic phases respectively. Meanwhile, the middle peak should be linked to the

composite hardness (i.e. imprints probing effective two-phase regions). Qualitatively similar histograms have been obtained for the other two cermets. Mean as well as standard deviation values for small-scale hardness for the three defined mechanically phases, determined by implementing the statistical method proposed by Ulm and co-workers [25,38–41], are listed in **Table 5.**

Two interesting observations may be done regarding the data presented in **Table 5**. First, and as expected, mean value of hardness for Ti(C,N) particles is determined to be about 34 GPa for the three materials, pointing out it is independent of microstructure and volume fraction of the ceramic phase. Second, opposite to this finding, values of local hardness for both composite-like and metallic phases are found to increase as the ceramic/metal phase ration rises. Here, relatively differences are relatively minor for the former, and possibly linked to the variable amount of ceramic particles. However, small-scale hardness values are significantly distinct for the metallic binder, indicating the relevance of the constrained deformation imposed for the harder phase to the softer and more ductile one, as it will be discussed now.

Details of binder peaks and data gathered in the lower-side range of the histograms are given in **Figure 9**. It is evidenced that small-scale hardness of the metallic phase rises about twice (from 9 to 19 GPa) as its mean free path reduces about half (from 1 to 0.5 microns). This is similar to the trend reported by Roa *et al.* [27] on WC-Co grades, and must be associated with the constraining effect of the ceramic phase over the metallic ones. However, before further discussing microstructure-mechanical property correlations,

special care should be taken on the reliability of the absolute values listed in **Table 5**. As it may be seen in **Figure 10a** and **Figure 10b,** for samples with 15 and 20 vol.% of FeNi, most of the imprints probing the metallic phase could not be completely confined in the corresponding binder mean free path. This was not the usual case for samples with 30 vol.% of metallic binder (**Figure 10c**). Consequently, the plastic flow associated with binder-related nanoindentations could be expected to interact with the surrounding ceramic particles. Under these conditions, assessed hardness values for the binder may be overestimated. As proposed and validated by Roa et al. [25], a more realistic value of intrinsic hardness for the constrained FeNi binder may be deconvoluted from the experimental values by implementing established thin film models. The use of thin films model is expected to yield reasonable values of hardness as the lateral stiffness is considered low in comparison to the normal stiffness, due to the large opening angle of the Berkovick tip. In this work Korsunsky *et al.´*s method [44] was implemented, resulting in hardness reductions of about 22% for 85Ti(C,N)-15FeNi and 80Ti(C,N)-20FeNi samples, and 12% for 70Ti(C,N)-30FeNi ones (**Table 6**).

The binder mean free path is a normalizing microstructural parameter in two-phase alloys. From a mechanical viewpoint, considering systems containing different phases (i.e. one hard and another soft) bound by a strong interface, it usually translates into constrained deformation of the soft phase due to the surrounding hard one. As a result, effective flow stress of the ductile phase is significantly enhanced. An estimation of this parameter for the FeNi binder may be done through simple conversion of previously estimated intrinsic hardness data, i.e. using Tabor's equation. In doing so, both a constraint factor ranging

between 3 and 4 (as reported for cemented carbides [45]), as well as a correction one of 0.9, related to the Berkovich indenter geometry instead of Vickers tip for measurement of mechanical properties [46], are considered. Resulting flow stress values for the three composites studied are also listed in **Table 6**. In general, they are within the range of values (from 1.8 to 4.5 GPa) reported for WC-Co cemented carbides [25,27,28,32,47,48], highlighting the potential of FeNi binder as effective reinforcement for Ti(C,N)-base cermets.

3.3. Deformation, damage and fracture mechanisms

Cermets demonstrate brittle fracture behaviour at macroscale, while both brittle features in the ceramic phase and ductile ones in the metallic binder phase can be distinguished at the microscale [49]. **Figure 11a** displays a FESEM micrograph of an imprint left after indentation down to high penetration depth in a 85Ti(C,N)-15FeNi specimen. Under these conditions, deformation/damage scenario is clearly involving the whole composite system. As it is shown in **Figure 11b**, damage within the residual imprint is mainly localized in Ti(C,N) ceramic particles (labelled with white arrows in **Figure 11b**). On the other hand, plastic deformation is evidenced within the binder, particularly in regions close to Ti(C,N)-FeNi interfaces. A more detailed inspection of fracture phenomena induced under the residual imprint during the indentation process was performed by cross-sectional analysis, by using FESEM/FIB, through the white dash line presented in **Figure11c.** A general view of the trench of the region of interest under the residual imprint is shown in **Figure 11d**,

which exhibits a highly deformed zone (underlined with a white dash line). Cracking induced is mainly located at ceramic/ceramic interfaces (indicated by white arrows).

As it can be appreciated in **Figure 12a** and **Figure 12b**, corresponding to imprints performed at a shallow penetration depth, same fracture mechanisms may be discerned inside the ceramic particles. Very interesting, cracks are found to propagate through the hard phase, but they often get arrested at the interface between Ti(C,N) particles and the metallic binder. This could be described as clear indication of the toughening role played by the ductile metallic binder, in terms of increasing crack-growth resistance in these ceramic-metal composites.

Evidence of similar toughening mechanisms as those reported for WC-Co grades is key for effective consideration of any alternative ceramic-metal systems as candidates to substitute hardmetals. In this regard, crack-microstructure interaction must be examined aiming to assess whether ductile reinforcement indeed takes place. **Figure 13a** shows typical cracking phenomena resulting at corners of residual imprints after Vickers indentation (in this case under applied load of 30 Kgf) on the hardest grade here studied. It can be seen that interaction of cracks induced by sharp indentation with microstructure is complex, combining transgranular, intergranular and through binder paths. Regarding the latter, the effectiveness of the metallic binder as a toughening agent is clearly discerned in terms of: smaller crack opening (red dashed circles in **Figure 13b**) and crack arrest in metallic binder pools, the latter sometimes inducing crack bifurcation (yellow dashed circles in **Figure 13b**). Above statement is further supported by fractographic inspection of broken surfaces

of previously indented specimens. As it is shown in **Figure 14**, as cracks go through the metallic phase and rupture takes place, well-developed ductile dimple features are left behind. This is by itself a clear proof of ligament reinforcement being operative, by reducing the driving force for crack propagation, towards effective toughening of the composite. Nevertheless, the area fraction of the metallic phase on fracture surfaces seems to be lower than expected, considering as a reference the metal/ceramic phase content defined during processing and later quantified by microstructural characterization. This would point out the need for microstructural design optimization in the studied systems, if the interaction between propagating cracks and the interdispersed metallic network acting as reinforcement phase wants to be enhanced.

4. Conclusions

The mechanical properties at microstructural length scale of Ti(C,N)-FeNi ceramic-metal composites have been assessed. Based on the obtained data, the following conclusions may be drawn:

1. Combination of massive nanoindentation and statistical analysis of the gathered data has proven to be a successful testing protocol for determining small-scale hardness and stiffness of Ti(C,N)-FeNi ceramic-metal composites. Nevertheless, successful implementation requires careful consideration of testing parameters used, on the basis of microstructural, residual imprint and plastic flow length scales.

2. The implemented testing protocol has allowed to document an inverse relationship between the mechanical parameters evaluated and the volume fraction of the metallic phase. For the particular case of the small-scale hardness of the metallic binder, such correlation has been analysed and rationalized in terms of strengthening of ductile ligaments due to constrained deformation by the surrounding ceramic particles.

3. The effective flow stress for the constrained metallic binder have been estimated from small-scale hardness values experimentally determined. It has yielded values ranging from 1.8 to 4.5 GPa, i.e. similar to those usually reported for cobalt

ligaments in WC-Co systems. This points out the effectiveness of FeNi as reinforcement phase for Ti(C,N)-base cermets, towards optimization of hardness-toughness relationships for these ceramic-metal systems.

4. Toughening action of FeNi phase in the Ti(C,N)-base cermets studied has been validated by detailed characterization of deformation, damage and fracture mechanisms. In particular, enhanced crack growth resistance has been discerned in terms of smaller opening, arrest and bifurcation of propagating cracks as they intersect metallic regions.

Acknowledgment

The current study was supported by the Spanish *Ministerio de Economía y Competitividad* through Grant MAT2015-70780-C4-P (MINECO/FEDER). J.J.Roa acknowledges the Serra Hunter programme of the Generalitat de Catalunya.

References

[1] H.E. Exner, Physical and chemical nature of cemented carbides, Int. Met. Rev. 24 (1979) 149–173. doi:10.1179/imtr.1979.24.1.149.

[2] G.S. Upadhyaya, Cemented tungsten carbides: production, properties and testing, William Andrew, 1998.

[3] J. Gurland, New scientific approaches to development of tool materials, Int. Mater. Rev. 33 (1988) 151–166. doi:10.1179/imr.1988.33.1.151.

[4] E. Jiménez-Piqué, M. Turon-Vinas, H. Chen, T. Trifonov, J. Fair, E. Tarrés, L. Llanes, Focused ion beam tomography of WC-Co cemented carbides, Int. J. Refract. Met. Hard Mater. 67 (2017) 9–17.

[5] J. García, V.C. Ciprés, A. Blomqvist, B. Kaplan, Cemented carbide microstructures: a review, Int. J. Refract. Met. Hard Mater. 80 (2019) 40–68.

[6] L. Prakash, Fundamentals and general applications of hardmetals, in: V.K. Sarin, D. Mari, L. Llanes (Eds.), Compr. Hard Mater., Elsevier Ltd, Oxford, UK, 2014: pp. 29–90.

[7] B. Gries, L.J. Prakash, Hard Materials 1: Acute Inhalation Toxicity by Contact Corrosion-The Case of WC-Co, in: Eur. Congr. Exhib. Powder Metall. Eur. PM Conf. Proc., The European Powder Metallurgy Association, 2007: p. 189.

[8] National Toxicology Program. Department of health and human service, (n.d.). http://ntp.niehs.nih.gov/?objectid=03C9AF75-E1BF-FF40-DBA9EC0928DF8B15, in, USA.

[9] M. Grilli, T. Bellezze, E. Gamsjäger, A. Rinaldi, P. Novak, S. Balos, R. Piticescu, M. Ruello, Solutions for critical raw materials under extreme conditions: a review, Materials (Basel). 10 (2017) 285.

[10] P. Ettmayer, H. Kolaska, W. Lengauer, K. Dreyer, Ti(C,N) Cermets - Metallurgy and Properties, Int. J. Refract. Met. Hard Mater. . 13 (n.d.).

[11] A. Bellosi, R. Calzavarini, M.G. Faga, F. Monteverde, C. Zancolò, G.E. D'Errico, Characterisation and application of titanium carbonitride-based cutting tools, J. Mater. Process. Technol. 143–144 (2003) 527–532. doi:http://dx.doi.org/10.1016/S0924-0136(03)00339-X.

[12] Y. Peng, H. Miao, Z. Peng, Development of TiCN-based cermets: Mechanical properties and wear mechanism, Int. J. Refract. Met. Hard Mater. 39 (2013) 78–89.

[13] Q. Xu, J. Zhao, X. Ai, Fabrication and cutting performance of Ti (C, N)-based cermet tools used for machining of high-strength steels, Ceram. Int. 43 (2017) 6286–6294.

[14] B. Wittmann, W.-D. Schubert, B. Lux, WC grain growth and grain growth inhibition in nickel and iron binder hardmetals, Int. J. Refract. Met. Hard Mater. 20 (2002) 51–60. doi:http://dx.doi.org/10.1016/S0263-4368(01)00070-1.

[15] E. Gordo, B. Gómez, E.M. Ruiz-Navas, J.M. Torralba, Influence of milling parameters on the manufacturing of Fe–TiCN composite powders, J. Mater. Process. Technol. 162–163 (2005) 59–64. doi:http://dx.doi.org/10.1016/j.jmatprotec.2005.02.154.

[16] B. Gries, L. Prakash, WC hardmetals with Iron based binders, in: P. Rödhammer, L. Sigl, H. Wildner, Proceedings of 17th Plansee Seminar, Reutte, Austria, 2009: p. HM 5/1-HM 5/13.

[17] P. Alvaredo, M. Dios, B. Ferrari, E. Gordo, Understanding of wetting and solubility behavior of Fe binder on Ti (C, N) cermets, J. Alloys Compd. 770 (2019) 17–25.

[18] A. V Shatov, S.S. Ponomarev, S.A. Firstov, Hardness and deformation of hardmetals at room temperature, in: V.K. Sarin, D. Mari, L. Llanes (Eds.), Compr. Hard Mater., Elsevier Ltd, Oxford, UK, 2014: pp. 267–299.

[19] A. V Shatov, S.S. Ponomarev, S.A. Firstov, Fracture and strength of hardmetals at room temperature, in: V.K. Sarin, D. Mari, L. Llanes (Eds.), Compr. Hard Mater., Elsevier Ltd, Oxford, UK, 2014: pp. 301–343.

[20] W. Lengauer, F. Scagnetto, Ti (C, N)-Based Cermets: Critical review of achievements and recent developments, in: Solid State Phenom., Trans Tech Publ, 2018: pp. 53–100.

[21] J.-H. Kim, Y. Kim, Influence of Mo contents on microstructures and mechanical properties of (Ti, W, Mo)(CN)–Ni cermets, Ceram. Int. 45 (2019) 5361–5366.

[22] C. Chen, Z. Guo, S. Li, Y. Xiao, B. Chai, J. Liu, Microstructure and properties of WC-17Co cermets prepared using different processing routes, Ceram. Int. (2019).

[23] A. Duszová, R. Halgaš, M. Bľanda, P. Hvizdoš, F. Lofaj, J. Dusza, J. Morgiel, Nanoindentation of WC–Co hardmetals, J. Eur. Ceram. Soc. 33 (2013) 2227–2232.

[24] M. Trueba, A. Aramburu, N. Rodríguez, I. Iparraguirre, M.R. Elizalde, I. Ocaña, J.M. Sánchez, J.M. Martínez-Esnaola, "In-situ" mechanical characterisation of WC–Co hardmetals using microbeam testing, Int. J. Refract. Met. Hard Mater. 43 (2014) 236–240.

[25] J.J. Roa, E. Jimenez-Pique, C. Verge, J.M. Tarragó, A. Mateo, J. Fair, L. Llanes, Intrinsic hardness of constitutive phases in WC–Co composites: Nanoindentation testing, statistical analysis, WC crystal orientation effects and flow stress for the constrained metallic binder, J. Eur. Ceram. Soc. 35 (2015) 3419–3425. doi:http://dx.doi.org/10.1016/j.jeurceramsoc.2015.04.021.

[26] T. Csanádi, M. Bl'anda, N.Q. Chinh, P. Hvizdoš, J. Dusza, Orientation-dependent hardness and nanoindentation-induced deformation mechanisms of WC crystals, Acta Mater. 83 (2015) 397–407.

[27] J.J. Roa, E. Jiménez-Piqué, J.M. Tarragó, D.A. Sandoval, A. Mateo, J. Fair, L. Llanes, Hall-Petch strengthening of the constrained metallic binder in WC–Co cemented carbides: experimental assessment by means of massive nanoindentation and statistical analysis, Mater. Sci. Eng. A. 676 (2016) 487–491.

[28] J.M. Tarragó, J.J. Roa, E. Jiménez-Piqué, E. Keown, J. Fair, L. Llanes, Mechanical deformation of WC–Co composite micropillars under uniaxial compression, Int. J. Refract. Met. Hard Mater. 54 (2016) 70–74.

[29] M.R. Elizalde, I. Ocaña, J. Alkorta, J.M. Sánchez-Moreno, Mechanical strength assessment of single WC-WC interfaces present in WC-Co hardmetals through micro-beam bending experiments, Int. J. Refract. Met. Hard Mater. 72 (2018) 39–44.

[30] D.A. Sandoval, A. Rinaldi, J.M. Tarragó, J.J. Roa, J. Fair, L. Llanes, Scale effect in mechanical characterization of WC-Co composites, Int. J. Refract. Met. Hard Mater. 72 (2018) 157–162.

[31] J.J. Roa, P.S. Phani, W.C. Oliver, L. Llanes, Mapping of mechanical properties at microstructural length scale in WC-Co cemented carbides: Assessment of hardness and elastic modulus by means of high speed massive nanoindentation and statistical analysis, Int. J. Refract. Met. Hard Mater. 75 (2018) 211–217.

[32] D.A. Sandoval, J.J. Roa, O. Ther, E. Tarrés, L. Llanes, Micromechanical properties of WC-(W, Ti, Ta, Nb) C-Co composites, J. Alloys Compd. 777 (2019) 593–601.

[33] J.A. Escribano, J.L. García, P. Alvaredo, B. Ferrari, E. Gordo, A.J. Sanchez-Herencia, FGM stainless steel-Ti (C, N) cermets through colloidal processing, Int. J. Refract. Met. Hard Mater. 49 (2015) 143–152.

[34] M. Dios, Z. Gonzalez, P. Alvaredo, R. Bermejo, E. Gordo, B. Ferrari, Novel colloidal approach for the microstructural improvement in Ti (C, N)/FeNi cermets, J. Alloys Compd. 724 (2017) 327–338.

[35] Metallographic Determination of Microstructure. Part 2: Measurement of WC Grain Size, in: ISO 4499-2 2008, Hardmetals, Geneva, 2008.

[36] W.C. Oliver, G.M. Pharr, An improved technique for determining hardness and elastic modulus using load and displacement sensing indentation experiments, J. Mater. Res. 7 (1992) 1564–1583. doi:10.1557/JMR.1992.1564.

[37] W.C. Oliver, G.M. Pharr, Measurement of hardness and elastic modulus by instrumented indentation: Advances in understanding and refinements to methodology, J. Mater. Res. 19 (2004) 3–20.

[38] G. Constantinides, F.-J. Ulm, K. Van Vliet, On the use of nanoindentation for cementitious materials, Mater. Struct. 36 (2003) 191–196. doi:10.1007/bf02479557.

[39] G. Constantinides, K.S. Ravi Chandran, F.J. Ulm, K.J. Van Vliet, Grid indentation analysis of composite microstructure and mechanics: Principles and validation, Mater. Sci. Eng. A. 430 (2006) 189–202. doi:http://dx.doi.org/10.1016/j.msea.2006.05.125.

[40] G. Constantinides, F.-J. Ulm, The nanogranular nature of C–S–H, J. Mech. Phys. Solids. 55 (2007) 64–90.

[41] F.-J. Ulm, M. Vandamme, C. Bobko, J. Alberto Ortega, K. Tai, C. Ortiz, Statistical Indentation Techniques for Hydrated Nanocomposites: Concrete, Bone, and Shale, J. Am. Ceram. Soc. 90 (2007) 2677–2692. doi:10.1111/j.1551-2916.2007.02012.x.

[42] B. Roebuck, P. Klose, K.P. Mingard, Hardness of hexagonal tungsten carbide crystals as a function of orientation, Acta Mater. 60 (2012) 6131–6143.

[43] W.D. Nix, H. Gao, Indentation size effects in crystalline materials: a law for strain gradient plasticity, J. Mech. Phys. Solids. 46 (1998) 411–425.

[44] A.M. Korsunsky, M.R. McGurk, S.J. Bull, T.F. Page, On the hardness of coated systems, Surf. Coatings Technol. 99 (1998) 171–183.

[45] H. Doi, Y. Fujiwara, K. Miyake, Mechanism of plastic deformation and dislocation damping of cemented carbides, Trans Met Soc AIME. 245 (1969) 1457–1470.

[46] O. Casals, J. Alcalá, The duality in mechanical property extractions from Vickers and Berkovich instrumented indentation experiments, Acta Mater. 53 (2005) 3545–3561.

[47] L.S. Sigl, H.F. Fischmeister, On the fracture toughness of cemented carbides, Acta Metall. 36 (1988) 887–897.

[48] H.F. Fischmeister, S. Schmauder, L.S. Sigl, Finite element modelling of crack propagation in WC-Co hard metals, Mater. Sci. Eng. A. 105 (1988) 305–311.

[49] M. Dios, I. Kraleva, Z. González, P. Alvaredo, B. Ferrari, E. Gordo, R. Bermejo, Mechanical characterization of Ti (C, N)-based cermets fabricated through different colloidal processing routes, J. Alloys Compd. 732 (2018) 806–817.

List of figures

Figure 6. (a) FESEM micrographs of a residual imprint performed at 200 nm of maximum displacement into surface performed inside the ceramic phase of sample 80Ti(C,N)-20FeNi; and (b) FIB-milled cross section of the same imprint, where plastic flow induced during the indentation process is marked with a black dash line.

Figure 7. FESEM micrograph image of small part of indentation array performed at 200 nm of maximum displacement into surface for sample 80Ti(C,N)-20FeNi.

Figure 8. Histogram of hardness values with constant bin size of 1 GPa, extracted from 2000 indentations for sample 85Ti(C,N)-15FeNi.

Figure 9. Histogram of hardness values for the metallic binder for all studied samples.

Figure 10. FESEM images of performed imprints on samples with different vol.% of metallic binder. (a) Sample 85Ti(C,N)-15FeNi, (b) sample 80Ti(C,N)-20FeNi, and (c) sample 70Ti(C,N)-30FeNi. The imprint, labelled by (*), has been performed and confined in the metallic binder. The white dash circle for Figure 10a/c represents the plastic field created during the indentation process.

Figure 11. (a) and (c): FESEM images of residual indentation imprints performed on the 80Ti(C,N)-20FeNi specimen. (b): Higher magnification image of residual imprint shown in (a), highlighting some fracture mechanisms activated during the indentation process (mainly within ceramic particles). (d): FIB-milled cross-section of residual imprint shown in (c), under the region of interest indicated by the white dash line.

Figure 12. (a) General view of a residual imprint performed at 200 nm of maximum displacement into surface; and (b) FIB-milled cross-section view, under the region of interest indicated by the white dash line in (a), for the 70Ti(C,N)-30FeNi specimen.

Figure 13. Cracking induced by sharp indentation in sample 85Ti(C,N)-15FeNi: a) imprint corresponding to Vickers indentation under 30kgf of applied load; and b) crack-microstructure interaction (enlarged view of red dashed area in (a)), highlighting toughening action linked to metallic phase in this composite system.

Figure 14. FESEM images from the fractured surface of sample 80Ti(C,N)-20FeNi. (a) ductile fracture within metallic binder, as evidenced by dimples clearly discerned in enlarged image (b).

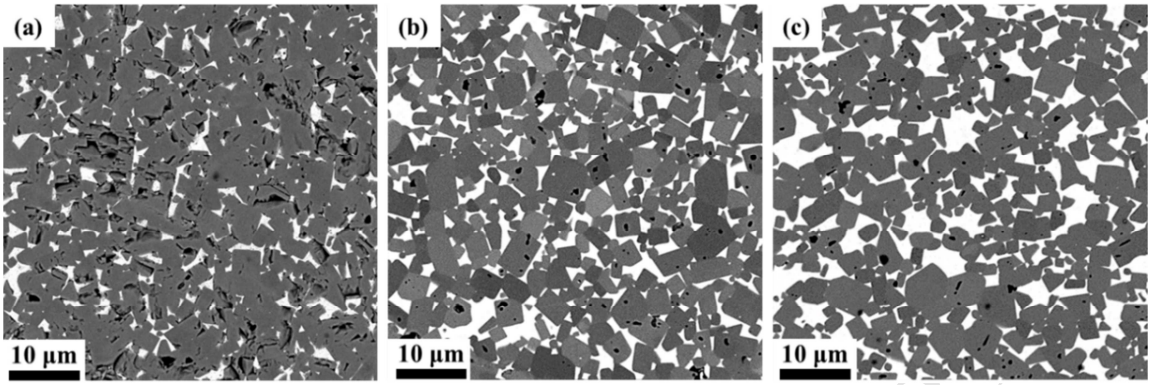

Figure 1. FESEM images of microstructure for Ti(C,N)-FeNi with different vol.% of the metallic binder: a) 85Ti(C,N)-15FeNi, b) 80Ti(C,N)-20FeNi and c) 70Ti(C,N)-30FeNi.

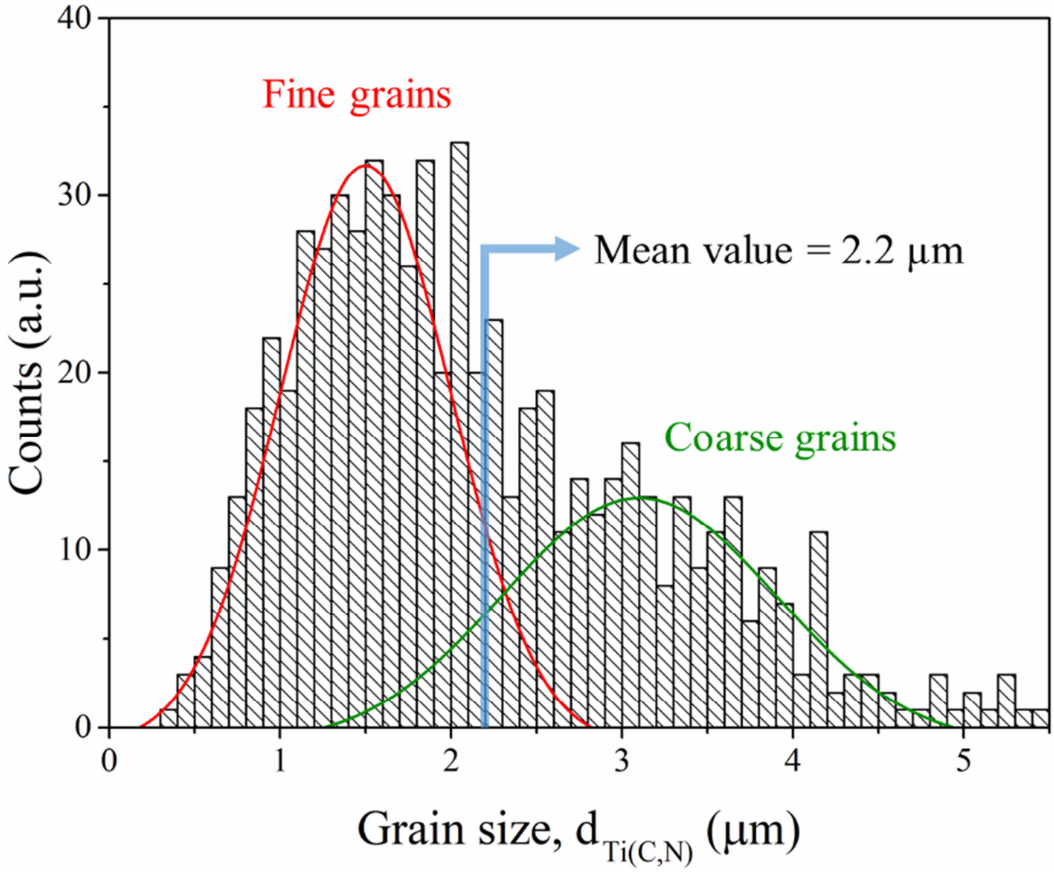

Figure 2. Grain size histogram for sample 85Ti(C,N)-15FeNi, with 100 nm of bin size. Two simulated distributions were fitted over the experimental values, as related to fine and coarse grains.

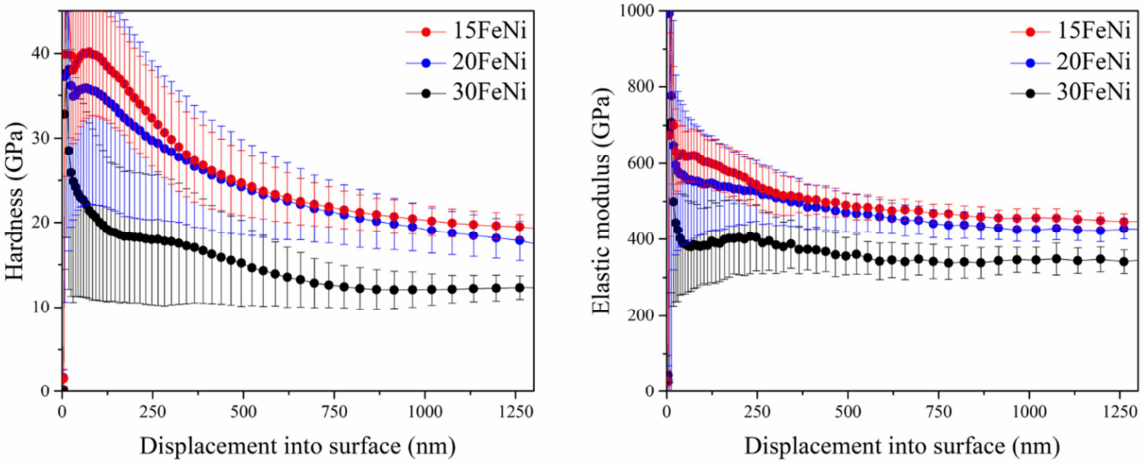

Figure 3. (a) *H* and (b) *E* evolution as a function of the maximum displacement into the surface for all the investigated samples.

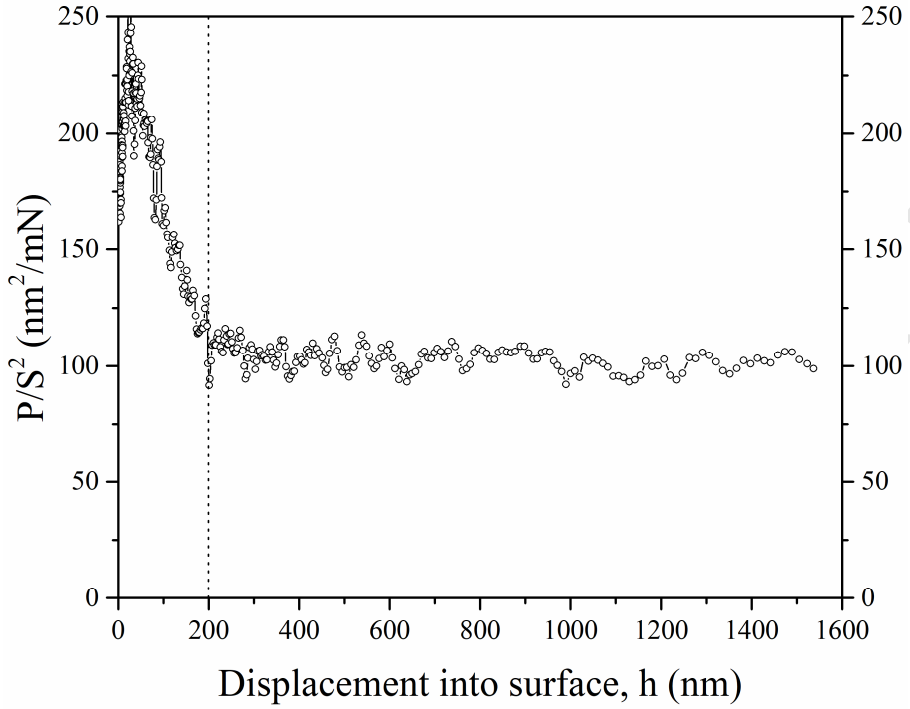

Figure 4. P/S^2 ratio versus displacement into surface for indentations performed at maximum applied load for sample 80Ti(C,N)-20FeNi.

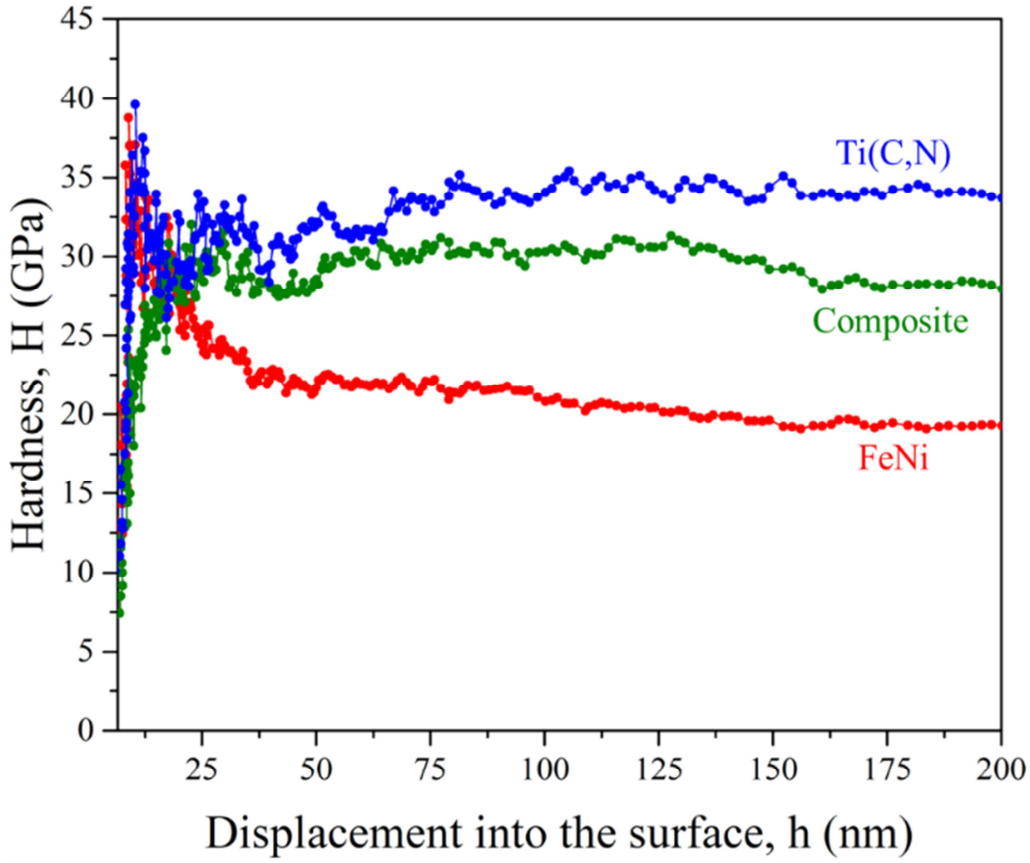

Figure 5. Hardness evolution as a function of the maximum displacement into the surface for each constitutive phase for the 80Ti(C,N)-20FeNi specimen.

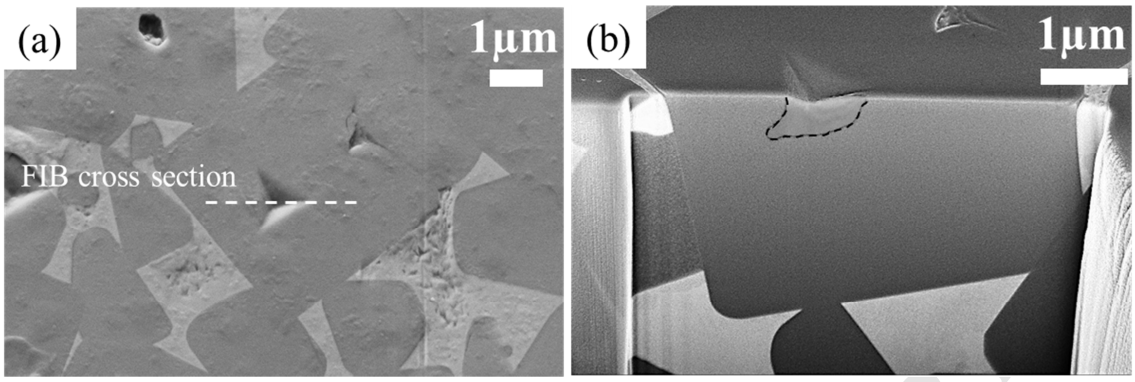

Figure 6. (a) FESEM micrographs of a residual imprint performed at 200 nm of maximum displacement into surface performed inside the ceramic phase of sample 80Ti(C,N)-20FeNi; and (b) FIB-milled cross section of the same imprint, where plastic flow induced during the indentation process is marked with a black dash line.

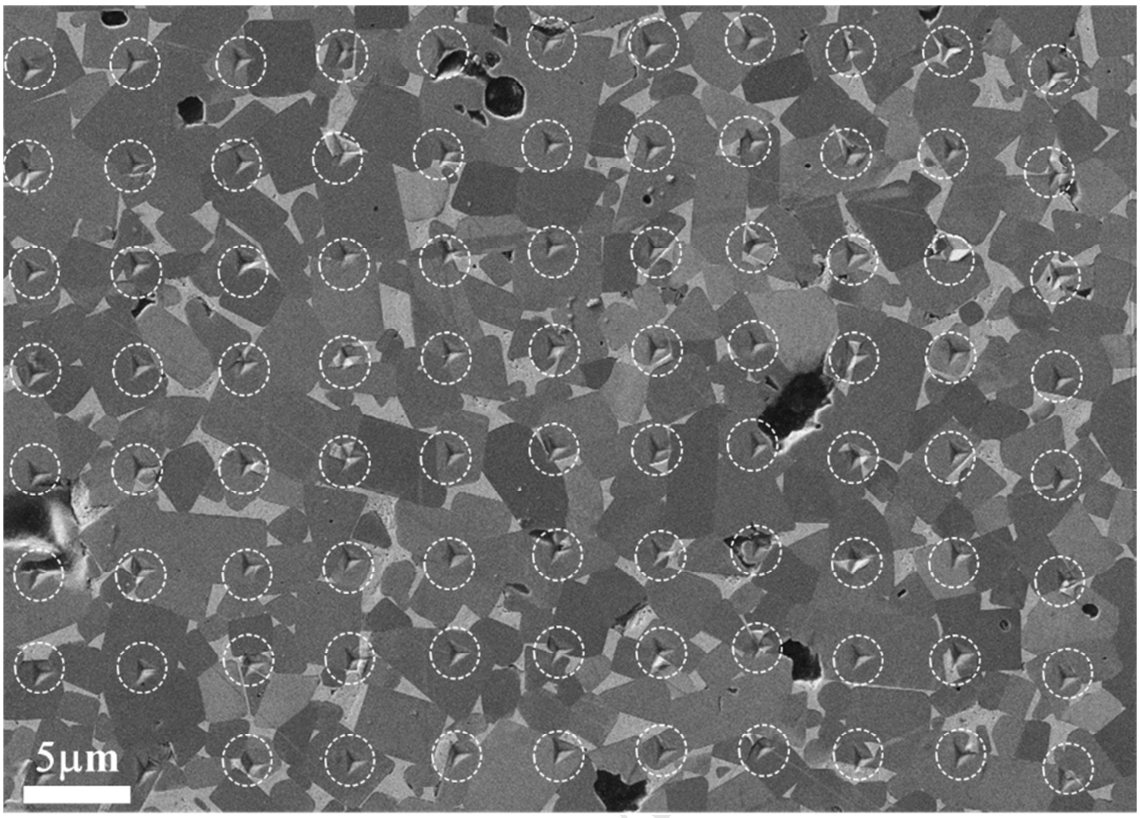

Figure 7. FESEM micrograph image of small part of indentation array performed at 200 nm of maximum displacement into surface for sample 80Ti(C,N)-20FeNi.

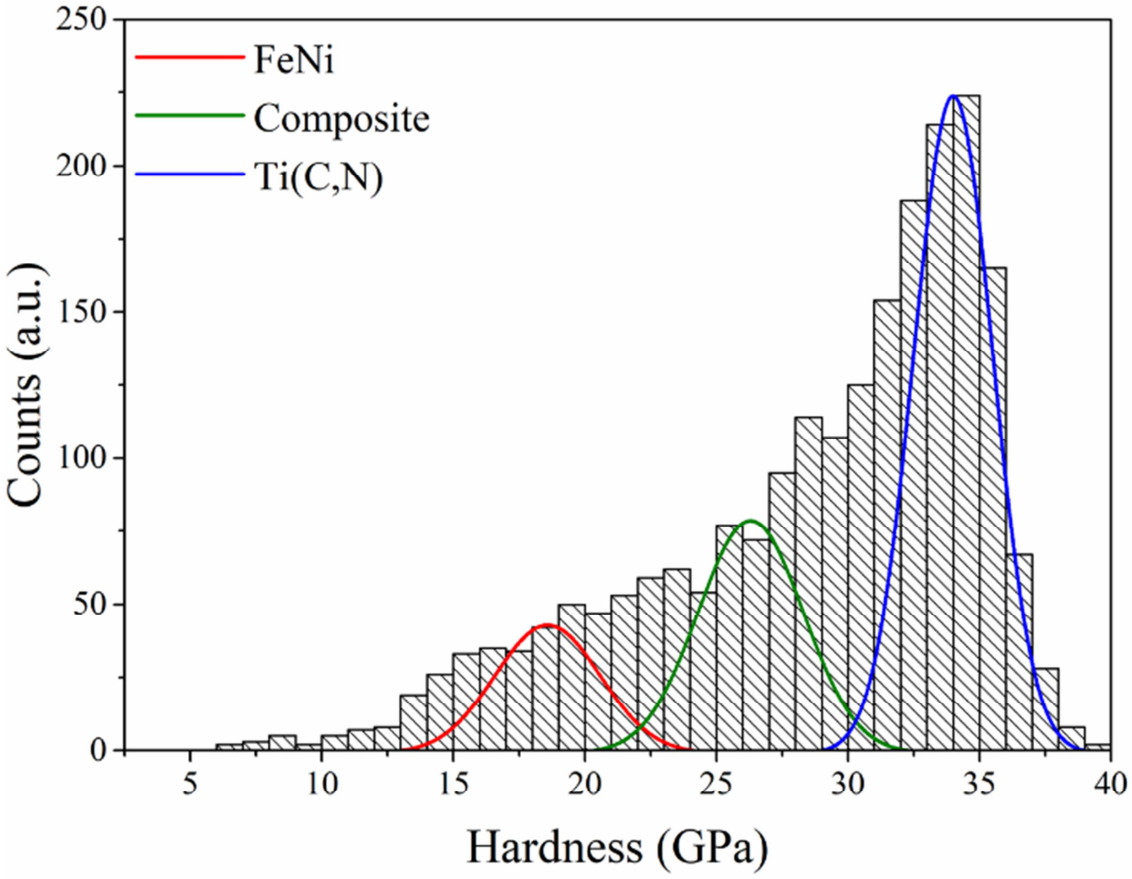

Figure 8. Histogram of hardness values with constant bin size of 1 GPa, extracted from 2000 indentations for sample 85Ti(C,N)-15FeNi.

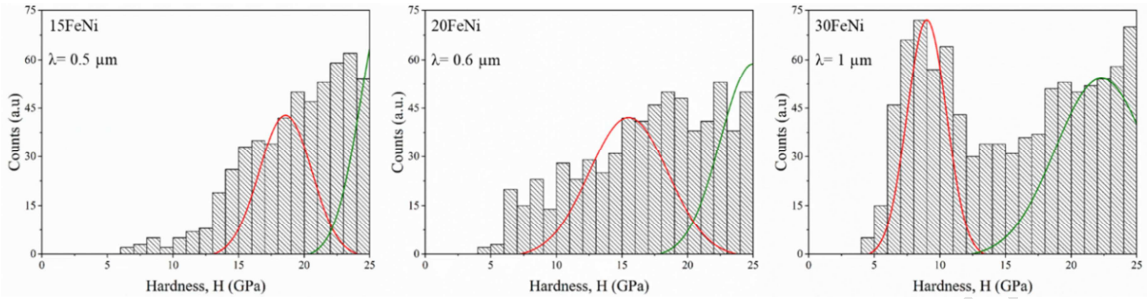

Figure 9. Histogram of hardness values for the metallic binder for all studied samples.

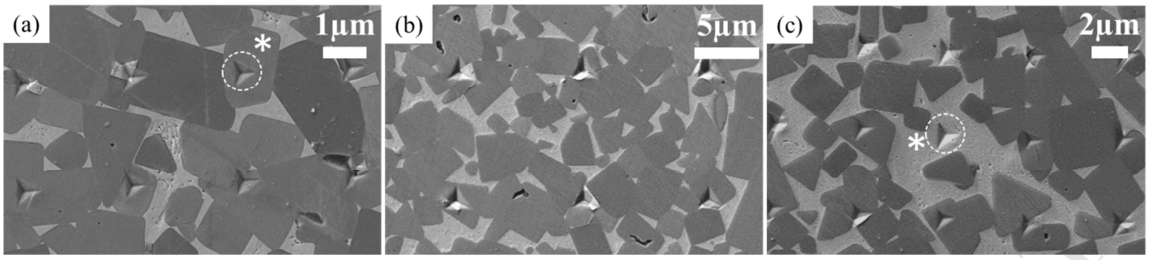

Figure 10. FESEM images of performed imprints on samples with different vol.% of metallic binder. (a) Sample 85Ti(C,N)-15FeNi, (b) sample 80Ti(C,N)-20FeNi, and (c) sample 70Ti(C,N)-30FeNi. The imprint, labelled by (*), has been performed and confined in the metallic binder. The white dash circle for **Figure 10 a/c** represents the plastic field created during the indentation process.

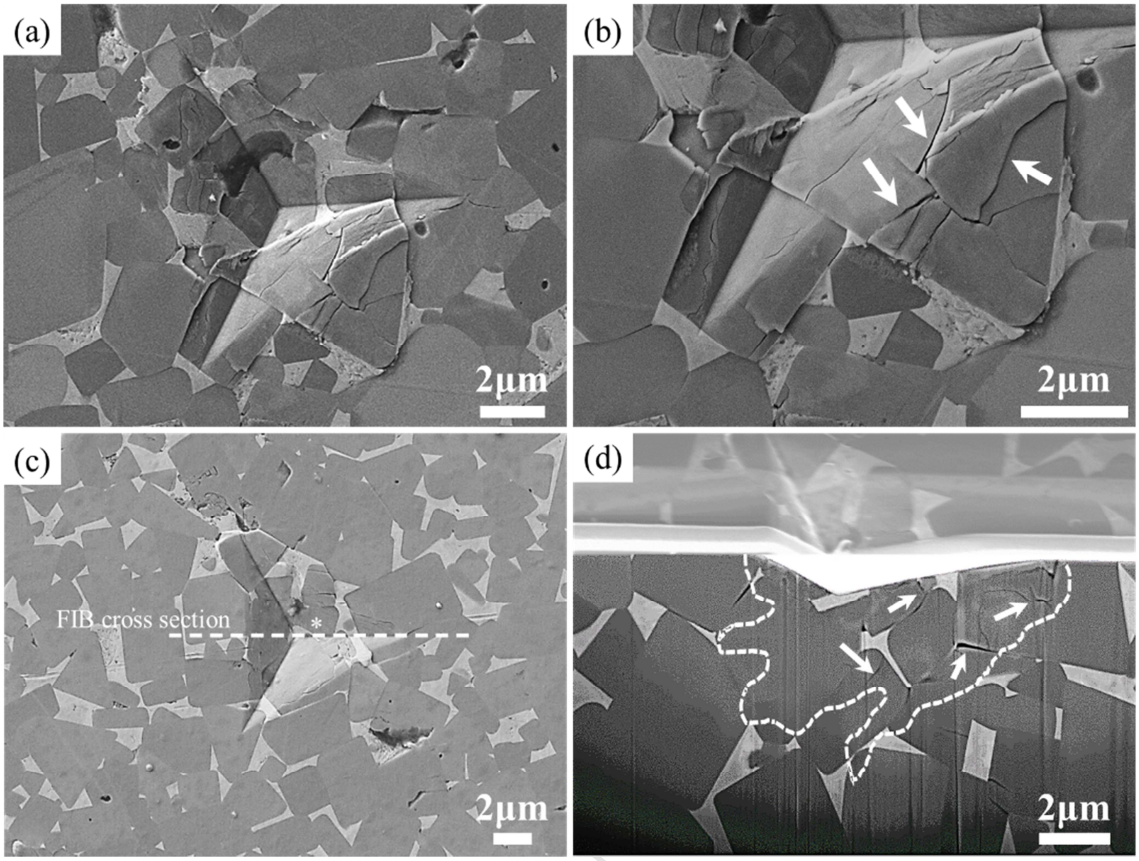

Figure 11. (a) and (c): FESEM images of residual indentation imprints performed on the 80Ti(C,N)-20FeNi specimen. (b): Higher magnification image of residual imprint shown in (a), highlighting some fracture mechanisms activated during the indentation process (mainly within ceramic particles). (d): FIB-milled cross-section of residual imprint shown in (c), under the region of interest indicated by the white dash line.

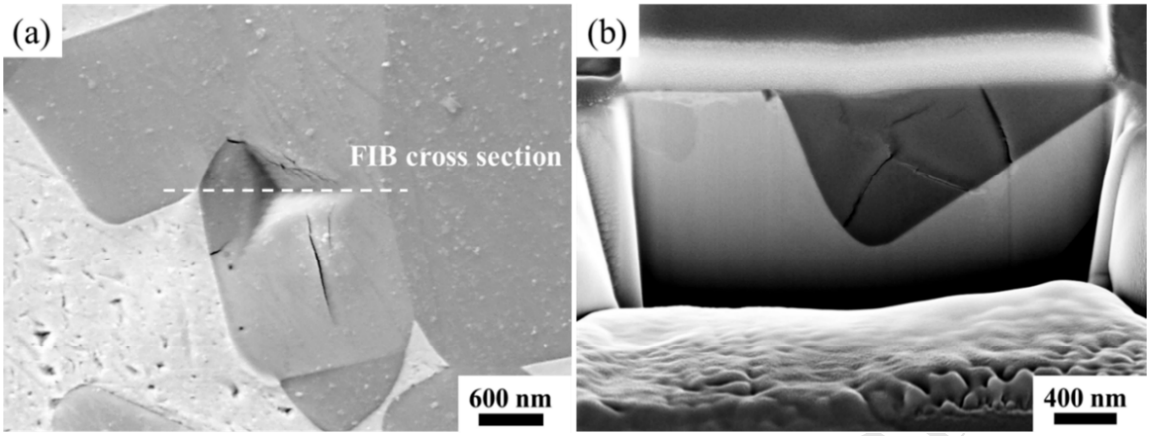

Figure 12. (a) General view of a residual imprint performed at 200 nm of maximum displacement into surface; and (b) FIB-milled cross-section view, under the region of interest indicated by the white dash line in (a), for the 70Ti(C,N)-30FeNi specimen.

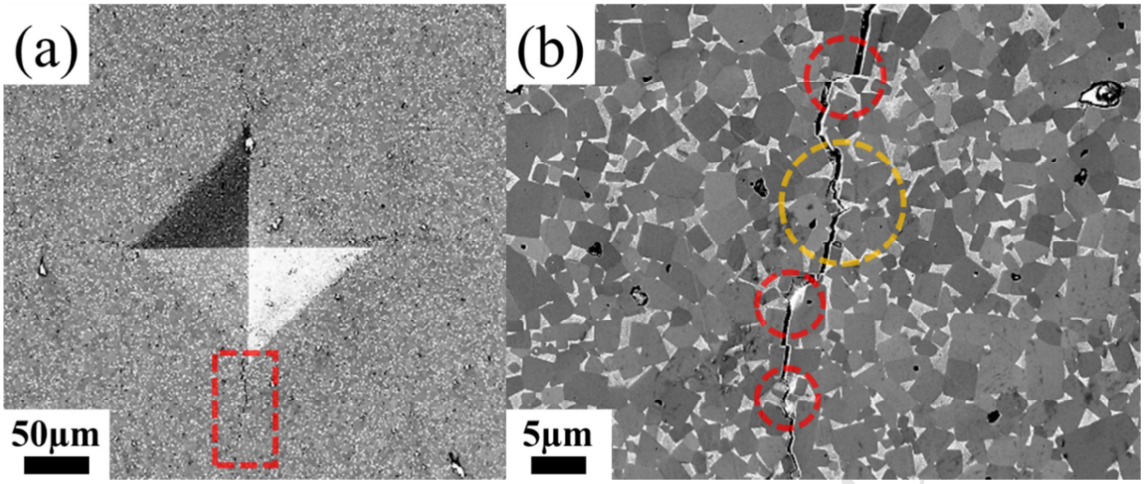

Figure 13. Cracking induced by sharp indentation in sample 85Ti(C,N)-15FeNi: a) imprint corresponding to Vickers indentation under 30kgf of applied load; and b) crack-microstructure interaction (enlarged view of red dashed area in (a)), highlighting toughening action linked to metallic phase in this composite system.

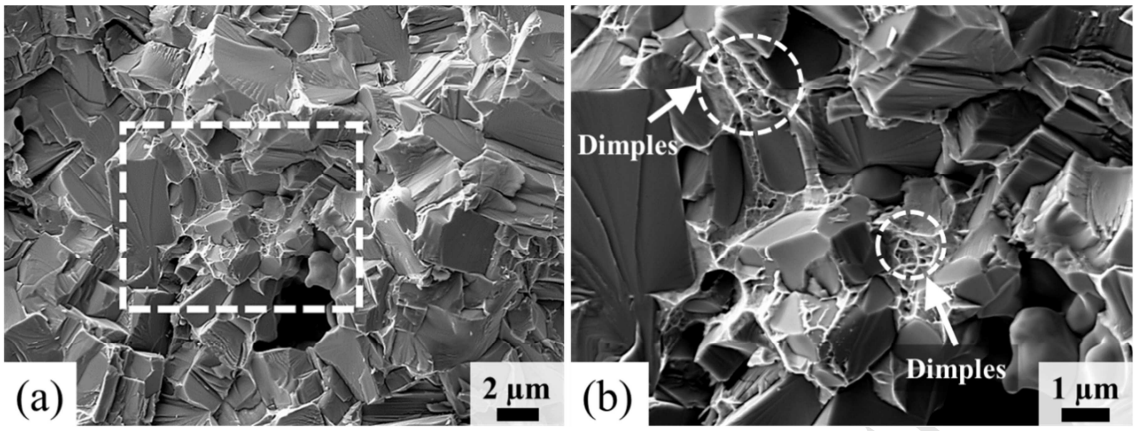

Figure 14. FESEM images from the fractured surface of sample 80Ti(C,N)-20FeNi. (a) ductile fracture within metallic binder, as evidenced by dimples clearly discerned in enlarged image (b).

List of tabels

Table 1. Physical characteristics for the as-received submicron powders.

Characteristics	Powder		
	Ti(C,N)	Fe	Ni
Density [a] ($g \cdot cm^{-3}$)	5.1	7.8	8.9
D_{v50} (μm)	2.1	3.5	1.7
Surface area [b] (m^2/g)	3.0	0.6	4.0

[a] ±0.1 Standard deviation in density measurements.

[b] ±0.1 Standard deviation in specific surface area measurements.

Table 2. Chemical formulation of suspensions.

Sample	Vol. %		wt. %		Composition metal matrix, wt. %	
	Ti(C,N)	Fe/Ni	Ti(C,N)	Fe/Ni	Fe	Ni
85Ti(C,N)-15FeNi	85	15	78.4	21.6	85	15
80Ti(C,N)-20FeNi	80	20	71.9	28.1		
70Ti(C,N)-30FeNi	70	30	59.9	40.1		

Table 3. Microstructural parameters of studied samples.

Sample name	Binder content, vol %	Mean Ti(C,N) grain size, $d_{Ti(C,N)}$ (μm)	Mean free path, λ (μm)	Porosity %
85Ti(C,N)-15FeNi	15	2.2 ± 0.3	0.5 ± 0.1	2.7 ± 1.1
80Ti(C,N)-20FeNi	20	2.2 ± 0.3	0.6 ± 0.1	0.5 ± 0.1
70Ti(C,N)-30FeNi	30	2.3 ± 0.3	1.0 ± 0.2	1.2 ± 0.9

Table 4. Mechanical properties data for the three different Ti(C,N)-FeNi composites studied in different length scale.

Sample	Nanoindentation data, performed by Berkovich indenter at 650 mN		HV10 (GPa)	HV30 (GPa)
	Elastic modulus, *E* (GPa)	Hardness, *H* (GPa)		
85Ti(C,N)-15FeNi	455 ± 20	20.2 ± 2.0	13.0 ± 0.4	12.8 ± 0.1
80Ti(C,N)-20FeNi	420 ± 18	18.5 ± 2.0	11.3 ± 0.3	11.0 ± 0.1
70Ti(C,N)-30FeNi	346 ± 22	12.3 ± 1.5	9.5 ± 0.4	9.1 ± 0.2

Table 5. Intrinsic hardness values (GPa) for each constitutive phase of Ti(C,N)-FeNi composite systems.

Sample	FeNi	Composite	Ti(C,N)
85Ti(C,N)-15FeNi	19.0 ± 0.5	26.3 ± 0.1	34.0 ± 1.0
80Ti(C,N)-20FeNi	15.5 ± 0.3	25.7 ± 0.2	34.0 ± 0.3
70Ti(C,N)-30FeNi	9.0 ± 0.1	22.3 ± 0.3	34.0 ± 0.3

Table 6. Corrected hardness values and flow stress (estimated by using Tabor's equation) of the metallic binder within Ti(C,N)-FeNi composites.

Sample	Binder Hardness (GPa)	Flow stress (GPa)
85Ti(C,N)-15FeNi	14.8 ± 0.4	3.4 – 4.5
80Ti(C,N)-20FeNi	12.1 ± 0.2	2.7 – 3.6
70Ti(C,N)-30FeNi	7.9 ± 0.1	1.8 – 2.4